

Anatomy-XNet: A Semi-Supervised Anatomy Aware Convolutional Neural Network for Thoracic Disease Classification

Uday Kamal, Mohammad Zunaed, Nusrat Binta Nizam, and Taufiq Hasan, *Senior Member, IEEE*

Abstract—Thoracic disease detection from chest radiographs using deep learning methods has been an active area of research in the last decade. Most previous methods attempt to focus on the diseased organs of the image by identifying spatial regions responsible for significant contributions to the model’s prediction. In contrast, expert radiologists first locate the prominent anatomical structures before determining if those regions are anomalous. Therefore, integrating anatomical knowledge within deep learning models could bring substantial improvement in automatic disease classification. Motivated by this, we propose Anatomy-XNet, an anatomy-aware attention-based thoracic disease classification network that prioritizes the spatial features guided by the pre-identified anatomy regions. We adopt a semi-supervised learning method by utilizing available small-scale organ-level annotation to localize the anatomy regions in large-scale datasets where the organ-level annotations are absent. The proposed Anatomy-XNet uses the pre-trained DenseNet-121 as the backbone network with two corresponding structured modules, the Anatomy Aware Attention (AAA) and Probabilistic Weighted Average Pooling (PWAP), in a cohesive framework for anatomical attention learning. We experimentally show that our proposed method sets a new state-of-the-art benchmark by achieving an AUC score of 85.66%, 91.13%, and, 84.04% on three publicly available large-scale CXR datasets—NIH, Stanford CheXpert, and MIMIC-CXR, respectively. This not only proves the efficacy of utilizing the anatomy segmentation knowledge to improve the thoracic disease classification but also demonstrate the generalizability of the proposed framework.

Index Terms—Thoracic disease classification, chest radiography, semi-supervised learning, anatomy-aware attention.

I. INTRODUCTION

CHEST radiography (CXR) is the most commonly used primary screening tool for assessing thoracic diseases such as pneumonia, pneumothorax, pulmonary edema, consolidation, infiltration, emphysema, and pleural effusions [1]. Each year a massive number of CXRs are produced, and the diagnosis is performed mainly by radiologists. Diagnosis of CXRs requires a high degree of skills and concentration. With the severe shortage of expert radiologists, especially in developing countries, computer-aided disease detection from chest radiographs is considered the future of medical diagnosis [2], [3]. Advancement in deep learning and artificial intelligence offers several ways of rapid, accurate, and reliable screening techniques [4]. These techniques can significantly impact the

Uday kamal, Mohammad Zunaed, Nusrat Binta Nizam, and Taufiq Hasan are with the Department of Biomedical Engineering, Bangladesh University of Engineering and Technology, Dhaka-1205, Bangladesh. (e-mails: uddy2014@gmail.com, rafizunaed@gmail.com, nusratbintanizam023@gmail.com, taufiq@bme.buet.ac.bd.)

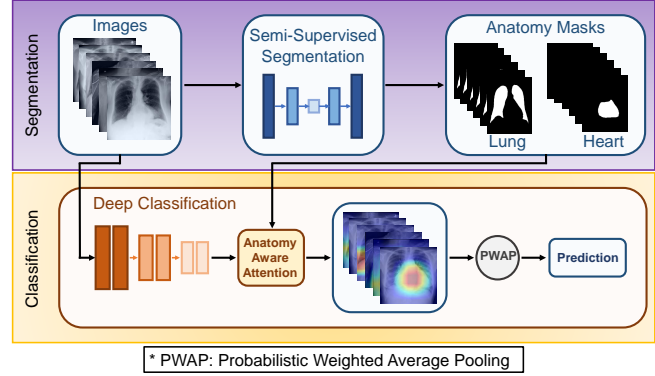


Fig. 1: Overview of the proposed semi-supervised anatomy-aware attention-based thoracic disease classification framework. A semi-supervised technique is utilized to generate anatomy masks for unannotated CXR images. Then, with the help of our proposed novel anatomy-aware attention module, anatomical information is integrated into the classification network for pathology detection.

health systems in the resource-constrained regions of the world where there is a high prevalence of thoracic diseases and a shortage of expert radiologists.

Driven by many publicly accessible large-scale CXR datasets, a significant amount of research efforts have been carried out for the automatic diagnosis of thoracic diseases. Wang *et al.* [5] first announced the ChestX-ray14 dataset and proposed a unified weakly-supervised classification network by introducing various multi-label DCNN losses based on ImageNet [6] pre-trained deep CNN models [7], [8], [9]. Tang *et al.* [10] used an attention-guided curriculum learning method to identify the disease category and localize the lesion areas. LLAGnet [11] is a novel lesion location attention guided network containing two corresponding attention modules which focus on the discriminative features from lesion areas for multi-label thoracic disease classification in CXRs. Guan *et al.* [12] proposed a category-wise residual attention learning (CRAL) framework for multi-label thoracic disease classification, which can suppress the obstacles of irrelevant classes by endowing small weights to the corresponding feature maps. In [13], Wang *et al.* proposed a DenseNet-121 based triple learning approach that integrates three attention modules which are unified for channel-wise, element-wise, and scale-wise attention learning.

In medical practice, interpretation of chest X-rays, or any other medical imaging modalities for that matter, requires an understanding of the relevant human anatomy that is being imaged. For example, fundamental analysis of chest X-rays involves the radiologist determining if the trachea is central, the lungs are uniformly expanded, the lung fields are clear, and the heart size is normal [14]. These and other similar observations form the basis of CXR interpretation by human vision, where it is clear that knowledge of anatomical structures is vital. However, most previous research works in automated analysis of CXRs do not consider this aspect and address the problem as any other computer vision problem. Most previous methods employed a global learning strategy [5], [15], or relied on attention mechanisms [10], [11], [16], that try to determine the spatial regions that are more responsible for model prediction. In [17], [18], [19], [20] methods have been proposed to integrate segmentation masks into the backbone framework. However, proper contour-level annotations for large-scale datasets [5], [21], [22] are unavailable. Generating segmentation mask from a minimal amount of annotated datasets (e.g., Japanese Society of Radiological Technology (JSRT) [23]) for these large-scale datasets lead to imperfect segmentation masks. However, the approaches in [17], [18], [19], [20], did not consider the effect of the imperfect segmentation masks in their proposed frameworks. These imperfections of the segmentation masks lead to difficulty for the backbone model to properly identify the anatomy regions. For thoracic disease classification, a lesion region is often associated with important anatomical regions, and therefore, incorporating anatomy-related information within deep learning models, along with the capability to handle the imperfection of the masks can potentially improve classification performance.

In this work, we propose an anatomy-aware attention-based architecture named Anatomy-XNet that utilizes the anatomy segmentation information along with CXRs frames to classify thoracic diseases. A significant challenge to integrate anatomy information into the framework is the lack of proper contour-level anatomy region annotations for large-scale datasets such as NIH [5], CheXpert [21], and MIMIC-CXR [22]. To solve this problem, we leverage a semi-supervised learning technique [24], requiring only a handful of annotated instances that enables us to utilize small scale dataset like JSRT [23] to train the segmentation network and generate the anatomy segmentation masks for the NIH, CheXpert, and MIMIC-CXR datasets. However, one downside of this method is that it doesn't guarantee similar performance compared to any supervised learning method [24]. In order to mitigate this problem, we incorporate two structured modules called Anatomy Aware Attention (AAA) and Probabilistic Weighted Average Pooling (PWAP) on top of Densenet-121 as the backbone feature extractor in a united framework. The AAA module not only reinforces the sensitivity of the different stages of the model to prioritize the anatomical location responsible for a thoracic disease, but also enables a relaxed view constraints on the imperfect anatomy mask. An overview of our proposed framework is presented in Fig. 1. The contributions of this paper are summarized as follows:

- We propose novel hierarchical feature-fusion-based AAA modules that learn to re-calibrate the feature maps in different stages of the model based on anatomy segmentation knowledge to improve the classification performance and improve the model's robustness to imperfection in anatomy segmentation.
- We incorporate novel PWAP modules that incorporates a learnable re-weighting mechanism based on spatial feature importance before performing spatial feature aggregation.
- Our proposed Anatomy-XNet achieves new state-of-the-art performances with AUC scores of 85.66%, 91.13%, and, 84.04% on three publicly available large-scale CXR datasets, NIH, Stanford CheXpert, and, MIMIC-CXR, respectively. These extensive experiments demonstrate the effectiveness of utilizing prior anatomy knowledge and prove the generalizability of the proposed framework.

II. RELATED WORK

A. Organ Segmentation from Chest Radiographs

There are several methods for organ segmentation from a CXR image. Among the classical signal processing based methods, a hybrid approach by Shao *et al.* [25] combining active shape and appearance models, a combined approach of landmark-based segmentation and a random forest classifier by Ibragimov *et al.* [26], an active shape framework addressing the initialization dependency of these active shape models proposed by Xu *et al.* [27] are noteworthy. In the advent of deep learning, Convolutional neural network (CNN) based segmentation of medical images has attracted wider attention of researchers. An end-to-end contour-aware CNN-based segmentation method is shown to provide organ contour information and improve the segmentation accuracy [28]. In [29], lung segmentation is performed from CXRs using Generative adversarial networks (GAN). However, this model is not generalizable to new datasets. Two-stage deep learning techniques such as patch classification and reconstruction of lung fields can be used for lung segmentation from CXR images [30]. In [31], an adaptive preprocessing with CNN is used for the segmentation of lung on contrast-enhanced binarized images.

B. Disease Classification from Chest Radiographs without Utilizing Segmentation Masks

Many signal processing and deep learning approaches have been proposed to classify thoracic diseases in recent years. Wang *et al.* [5] utilized the ImageNet [6] pre-trained deep CNN models, i.e., AlexNet, VGGNet [7], GoogLeNet [8], ResNet [9], to perform multi-label thoracic disease classification. Yao *et al.* [32] proposed a joint variant of DenseNet [33] and Long-Short Term Memory Network (LSTM) [34] to focus on the label correlation among image labels. Wang *et al.* [35] proposed the TieNet (Text Image Embedding Network), an end-to-end CNN-RNN framework, for learning to embed visual images and text reports for image classification and report generation. Tang *et al.* [10] identified the disease category and localized the lesion areas through an attention-guided

curriculum learning method. In [36], multiple feature integration is presented using shallow handcrafted techniques and a pre-trained deep CNN model. The classification approach integrates four types of local and deep features extracted from SIFT, GIST, LBP, and HOG, and convolutional CNN features. DualCheXNet [37] is an approach that enables two different feature fusion operations, such as feature-level fusion (FLF) and decision level fusion (DLF), which form the complementary feature learning embedded in the network. LLAGNet [11] is a novel lesion location attention guided network containing two corresponding attention modules which focus on the discriminative features from lesion locations for multi-label thoracic disease classification in CXRs.

Guan *et al.* [12] proposed a category-wise residual attention learning (CRAL) framework for multi-label thoracic disease classification. CRAL alleviates irrelevant classes by assigning small weights to the corresponding feature representations. Rajpurkar *et al.* [15] exploited a modified 121-layer DenseNet named CheXNet, for diagnosis of all 14 pathologies in the ChestXray14 dataset, especially for “Pneumonia”. In [13], a triple learning approach integrating a unified channel-wise, element-wise, and scale-wise attention modules are used. They can simultaneously learn disease-discriminative channels, locations, and scales for effective diagnosis. Hou *et al.* [38] fused semantic features from radiology reports along with encoded X-ray features to feed into transformer encoder to utilize both CXR images and metadata related to them. Zhang *et al.* [39] proposed a medical concept graph, based on prior knowledge, to diagnose CXR images. In [40] Seyyed-Kalantar *et al.* examined the extent to which state-of-the-art deep learning classifiers show true positive rate disparity among different protected attributes and different datasets. Allaouzi *et al.* [41] explored binary relevance (BR), label powerset (LP), and classifier chain (CC) in terms of label dependencies. Yan *et al.* [16] proposed a weakly supervised deep learning framework equipped with the squeeze and excitation blocks, multi-map transfer, and max-min pooling for classifying thoracic diseases as well as localizing suspicious lesion regions. Luo *et al.* [42] adopted task-specific adversarial training and an uncertainty-aware temporal ensemble of model predictions to address the domain and label discrepancies across different datasets. To handle label uncertainty on the CheXpert dataset, Irvin *et al.* [21] trained a DenseNet-121 on CheXpert with various labeling policies such as U-Ignore, U-Ones, and U-Zeros policies. Pham *et al.* [43] exploits dependencies among abnormality labels and utilized label smoothing technique for better handling of uncertain samples in the CheXpert dataset. However, a systematic exploration of the potential of integrating anatomical prior to improve the classification performance was absent in all the above mentioned methods.

C. Disease Classification from Chest Radiographs Utilizing Segmentation Masks

Xu *et al.* [17] proposed a dual-stage approach (segmentation and classification) to utilize mask attention mechanism as spatial attention to adjust salient features of the CNN. Their attention mask suppresses the receptive field of the CNN

based on their overlapping rates with the segmentation masks. However, they did not consider the effect of the imperfection of the segmentation masks in their approach. Unavailability of the segmentation masks of large-scale datasets and imperfection in the segmentation masks due to supervised training on the small-scale dataset make their model susceptible to masking important features of different layers of the CNN. Keidar *et al.* [18] proposed a deep learning model for the detection of COVID-19 from CXRs. They incorporated the segmentation masks in the green channel of the input image. Segmentation-based Deep Fusion Network (SDFN) [19] is a method that leverages the domain knowledge and the higher-resolution information of local lung regions. The local lung regions are identified using Lung Region Generator (LRG), and discriminative features are extracted using two CNN models. Then these features are fused by the feature fusion module for the disease classification process. Daniel *et al.* [20] proposed a two-stage method where surroundings area around anatomy regions are removed from the CXR image based on the segmentation masks to remove any classification bias towards the extraneous (i.e., non-anatomy) regions of the image. Afterward, they fed the CXR image constrained by the segmentation mask to a CNN model. Overall, the methods described in [17], [18], [19] and [20] have utilized small-scale annotated datasets (e.g., JSRT) in a supervised training setting to generate segmentation masks for large-scale datasets used in their approaches. However, in these methods, the effect of imperfect segmentation masks was not considered, which naturally arises from supervised training of the segmentation network using out-of-distribution data resources.

III. METHODOLOGY

A. Motivation

Successful implementation of deep learning-based thoracic disease classification approaches requires not only higher accuracy but also interpretability. Real-world radiologists locate the vital anatomy regions first and then determine if those regions have abnormalities. None of the previous works discussed in Section II-B integrates anatomy knowledge into their framework. In this work, we aim to bridge this gap between human experts and the ML models by incorporating prior information of the anatomical regions into the network. However, the existing annotated anatomy segmentation datasets are very small in size. Using them in a supervised learning environment will limit the model’s generalizability. Thus, we leverage a semi-supervised learning technique [24] that can work on a minimal amount of annotated datasets (e.g., JSRT). However, the imperfect mask segmentation from the semi-supervised-based approach can pose a challenge to the classification network if they are passed as it is. Also, we can not perform segmentation of the vital anatomy regions (e.g., lung, heart) and provide only those regions as input to the network. This will constrain the field of view for the network and may lead to difficulty in learning to identify and differentiate the anatomy regions. Therefore, we propose an anatomy-aware attention-based architecture named Anatomy X-Net that integrates anatomy segmentation knowledge into

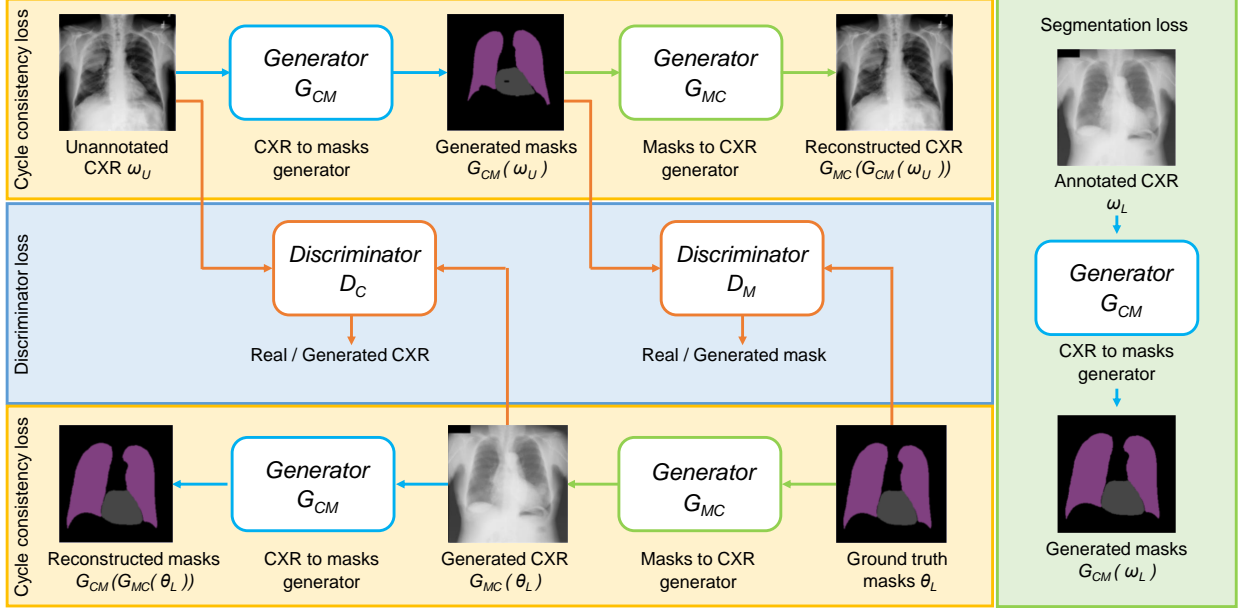


Fig. 2: Overview of the semi-supervised anatomy segmentation architecture. The pipeline contains four networks that are trained simultaneously.

different stages of the network to prioritize the spatial regions generally responsible for the pathologies.

B. Semi-supervised Anatomy Segmentation Network

For semi-supervised segmentation of anatomy regions, we adopted the method from [24] which is based on the popular CycleGAN architecture [44]. The CycleGAN architecture comprises of four interconnected blocks, two conditional generators, and two discriminators as illustrated in Fig. 2. The first generator (G_{CM}), corresponding to the segmentation network that we want to obtain, learns a mapping from a CXR image to its anatomy segmentation masks. The first discriminator (D_M) takes either the output generated mask from G_{CM} or the real segmentation mask as input, and learns to differentiate one from another. Conversely, the second generator (G_{MC}) learns to map a segmentation mask back to its CXR image. The second discriminator (D_C) receives a CXR image as input (either a real CXR image or an output generated CXR from G_{MC}) and predicts whether this image is real or generated. To enforce cycle consistency criterion, the segmentation network is trained in a way so that feeding the segmentation masks generated by G_{CM} for a CXR image into G_{MC} returns the same CXR image. Similarly, passing back the CXR image generated by G_{MC} to G_{CM} for a segmentation mask returns the same mask.

Loss functions:

In this section, we define the loss functions employed to train our model in a semi-supervised setting. The segmentation setting contains two distinct subsets: subset L , containing annotated CXR images ω_L and their corresponding ground-truth masks θ_L , and subset U , which contains unannotated CXR images ω_U . We train the generator module G_{CM} to

generate segmentation masks by imposing the following loss function,

$$\mathcal{L}_{gen}^M(G_{CM}) = \mathbb{E}_{\omega, \theta \in \omega_L, \theta_L} [\mathcal{H}(\theta, G_{CM}(\omega))] \quad (1)$$

where \mathcal{H} is the pixel-wise cross-entropy defined as,

$$\mathcal{H}(\theta, \tilde{\theta}) = - \sum_{j=1}^N \sum_{k=1}^K \theta_{j,k} \log \tilde{\theta}_{j,k} \quad (2)$$

where, $\theta_{j,k}$ and $\tilde{\theta}_{j,k}$ are the annotated segmentation masks and predicted probabilities that pixel $j \in \{1, \dots, N\}$ has label $k \in \{1, \dots, K\}$. Likewise, we employ a pixel-wise L2 norm between an annotated CXR and the CXR generated from its corresponding segmentation mask as a supervised loss to train the CXR generator G_{MC} :

$$\mathcal{L}_{gen}^C(G_{MC}) = \mathbb{E}_{\omega, \theta \in \omega_L, \theta_L} [\|G_{MC}(\theta) - \omega\|_2^2] \quad (3)$$

Two additional losses, adversarial and cycle consistency losses, are incorporated to exploit unannotated CXR images. We use the adversarial losses to train the generators and discriminators in a competing fashion and help the generators produce realistic CXR images and anatomy segmentation masks. Suppose that $D_M(\theta)$ is the predicted probability that segmentation masks θ correspond to an annotated CXR's segmentation mask. We define the adversarial loss for D_M as,

$$\begin{aligned} \mathcal{L}_{disc}^M(G_{CM}, D_M) = & \mathbb{E}_{\theta \in \theta_L} [(D_M(\theta) - 1)^2] + \\ & \mathbb{E}_{\omega' \in \omega_U} [(D_M(G_{CM}(\omega')))^2] \end{aligned} \quad (4)$$

Let $D_C(\omega)$ be the predicted probability that a CXR ω is real. We get the adversarial loss for the CXR discriminator by,

$$\begin{aligned} \mathcal{L}_{disc}^C(G_{MC}, D_C) = & \mathbb{E}_{\omega' \in \omega_U} [(D_C(\omega') - 1)^2] + \\ & \mathbb{E}_{\theta \in \theta_L} [(D_C(G_{MC}(\theta)))^2] \end{aligned} \quad (5)$$

The first cycle consistency loss measures the difference between an unannotated CXR and the regenerated CXR after passing through generators G_{CM} and G_{MC} sequentially.

$$\mathcal{L}_{cycle}^C(G_{CM}, G_{MC}) = \mathbb{E}_{\omega' \in \omega_U} [\|G_{MC}(G_{CM}(\omega')) - \omega'\|_1] \quad (6)$$

We use cross-entropy to evaluate the difference between an annotated and regenerated segmentation mask after passing through generators G_{MC} and G_{CM} in sequence:

$$\mathcal{L}_{cycle}^M(G_{CM}, G_{MC}) = \mathbb{E}_{\theta \in \theta_L} [\mathcal{H}(\theta, G_{CM}(G_{MC}(\theta)))] \quad (7)$$

Finally, the total loss is obtained by combining all six loss terms:

$$\begin{aligned} \mathcal{L}_{total}(G_{CM}, G_{MC}, D_M, D_C) = & \mathcal{L}_{gen}^M(G_{CM}) + \mathcal{L}_{gen}^C(G_{MC}) \\ & + \mathcal{L}_{cycle}^M(G_{CM}, G_{MC}) + \mathcal{L}_{cycle}^C(G_{CM}, G_{MC}) \\ & - \mathcal{L}_{disc}^M(G_{CM}, D_M) - \mathcal{L}_{disc}^C(G_{MC}, D_C) \end{aligned} \quad (8)$$

We perform the learning in an alternating fashion. The parameters of the generators are optimized while considering those of the discriminators as fixed and vice versa.

C. Anatomy-XNet

The proposed anatomy-aware thoracic disease classification network is illustrated in Fig. 3. We utilized transfer learning on DenseNet-121 [33] architecture pre-trained on the ImageNet [6] and used it as our backbone model. The backbone model compresses the raw pixel-level information present in a CXR image to a high-level feature of lower-dimensional space. DenseNet-121 consists of four dense blocks (DB). The proposed AAA attention module operates on the high-level feature space encoded by these DBs. AAA enforces attention supervision to the salient regions of the feature space guided by the anatomy segmentation masks. Due to hardware constraints, we performed downsampling and upsampling on the anatomy segmentation masks and feature space to an intermediate shape before passing them to an AAA module. These recalibrated feature spaces from each of the AAA modules are pooled by PWAP layers (post-AAA) and concatenated together. Finally, this concatenated feature vector is passed to a fully connected layer for pathology classification. The different components of the proposed Anatomy-XNet architecture is described in the following sub-sections.

Anatomy Aware Attention (AAA) Module:

The AAA module consists of a PWAP module (intra-AAA), attention vector encoders, and batch normalization layers. The anatomy-XNet consists of two AAA modules. The first AAA module is connected to the third dense block (DB-3), and the other AAA module works with the fourth dense block (DB-4). Each one of them takes the upsampled high-level feature maps $\mathbf{F}_{DB}^{US} \in \mathbb{R}^{H \times W \times C}$ generated by their corresponding DB block, and the downsampled anatomy segmentation masks $\mathbf{M} \in \mathbb{R}^{H \times W \times 2}$ as inputs. Using a PWAP module (intra-AAA), the feature map is pooled to a feature vector $\mathbf{V} \in \mathbb{R}^{1 \times 1 \times C}$. This feature vector \mathbf{V} is then passed through three different attention vector encoders to get the three feature vectors $\mathbf{A}_1, \mathbf{A}_2, \mathbf{A}_3 \in \mathbb{R}^{1 \times 1 \times C}$. The attention vector encoders are inspired by the “Squeeze-and-Excitation” (SE) block [45]. The detailed

architecture of an attention vector encoder module is described in the Table I. To introduce bottleneck, feature vector \mathbf{V} is first squeezed into dimension $1 \times 1 \times (C/r)$ and later excited back to $1 \times 1 \times C$. Here, r is the reduction ratio. For the first AAA module that is used on the upsampled feature map encoded by DB-3, the value of C is 512, and r is 0.5. The second AAA module is used on the upsampled feature space derived from the DB-4. For this module, C is 1024, and r is 0.5.

We aim to give relevant importance to lung and heart anatomy compared to background regions. One straightforward way is to apply softmax operation across all the attention vectors to get that relevancy scores. But one drawback of this approach is that it will make the attention scores for lung and heart attention vectors dependent on each other. However, pathologies related to the heart are independent of whether the CXR contains lung pathologies or not. This motivates us to design the softmax operations across the attention vectors in such a way that the lung attention vector and heart attention vector are independent of each other, but the background-suppressor attention vector is jointly dependent on both of them. First, we apply softmax between \mathbf{A}_1 and \mathbf{A}_2 , by,

$$\sigma(\mathbf{A}_k)_i = \frac{\exp(\mathbf{A}_k)_i}{\sum_{j=1}^2 \exp(\mathbf{A}_j)_i}, i \in \{1, \dots, C\}, k \in \{1, 2\} \quad (9)$$

Here, $\sigma(\cdot)$ represents softmax activation function, j and k represent feature vector indices, and i represents the i^{th} channel value of a feature vector. Thus, we obtain two attention vectors where each feature value across the channel dimension depends on each other. We name these two attention vectors as the lung enhancer and first background-suppressor denoted by \mathbf{A}_{LE} and $\mathbf{A}_{\overline{LE}}$, respectively. These quantities are related by,

$$(\mathbf{A}_{LE})_i + (\mathbf{A}_{\overline{LE}})_i = 1 \quad (10)$$

where, $i \in \{1, \dots, C\}$. Similarly, we apply softmax between \mathbf{A}_2 and \mathbf{A}_3 by,

$$\sigma(\mathbf{A}_k)_i = \frac{\exp(\mathbf{A}_k)_i}{\sum_{j=2}^3 \exp(\mathbf{A}_j)_i}, i \in \{1, \dots, C\}, k \in \{2, 3\} \quad (11)$$

Here, $\sigma(\cdot)$ represents softmax activation function, j and k represent feature vector indices, and i represents the i^{th} channel value of a feature vector. Similarly, we obtain two attention vectors where each feature value across the channel dimension depends on each other. We name these two attention vectors as the second background-suppressor and heart enhancer denoted by $\mathbf{A}_{\overline{HE}}$ and \mathbf{A}_{HE} , respectively. These quantities are related by,

$$(\mathbf{A}_{HE})_i + (\mathbf{A}_{\overline{HE}})_i = 1 \quad (12)$$

TABLE I: ATTENTION VECTOR ENCODER STRUCTURE.

Layer (Type)	Input Shape	Output Shape
FC-1 (Fully Connected)	(C)	(C/r)
ReLU-1 (ReLU)	(C/r)	(C/r)
BN-1 (Batch Normalization)	(C/r)	(C/r)
FC-2 (Fully Connected)	(C/r)	(C)
ReLU-2 (ReLU)	(C)	(C)
BN-2 (Batch Normalization)	(C)	(C)

* C: Channel Dimension r: Reduction ratio

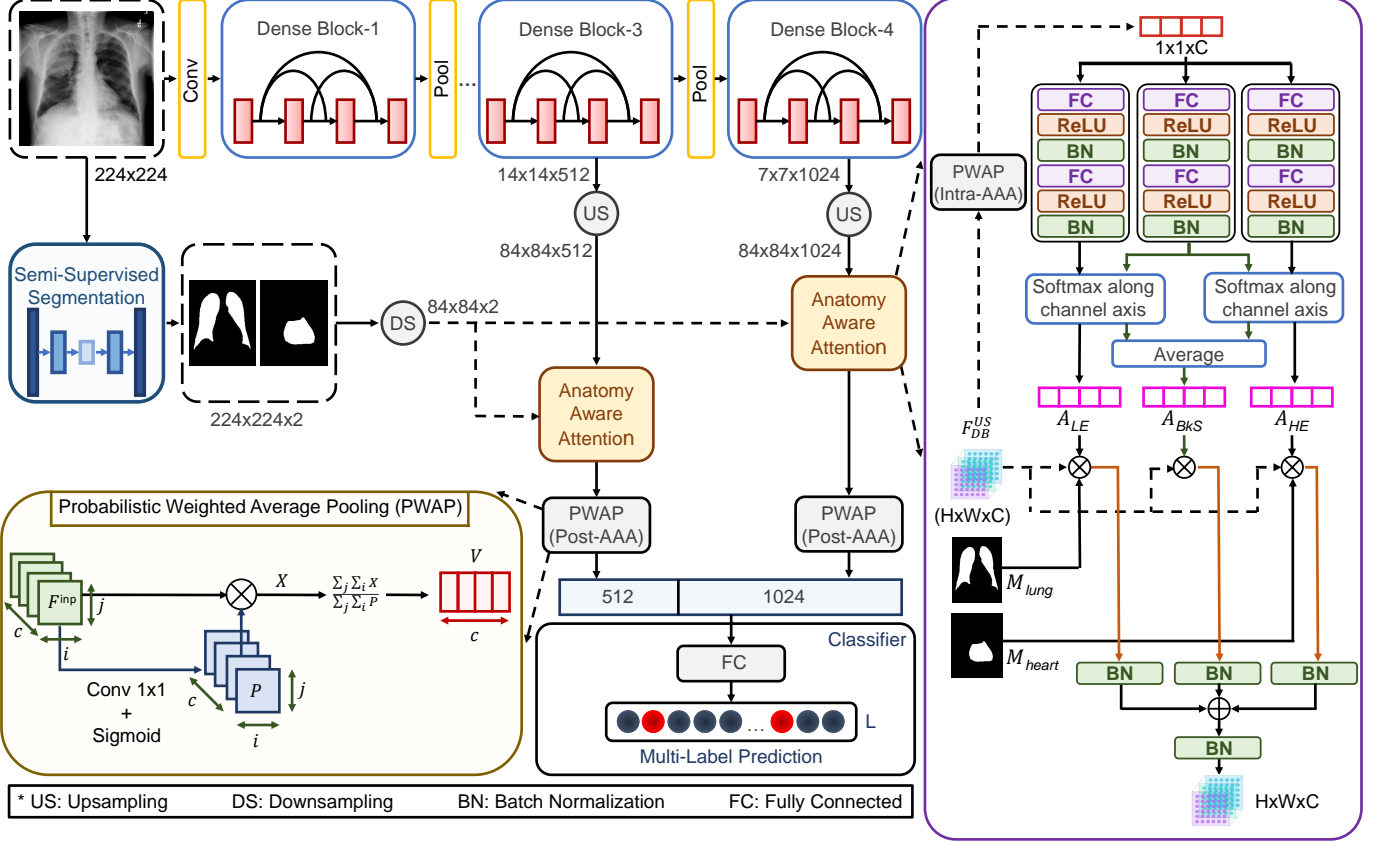


Fig. 3: The architecture of the proposed Anatomy-XNet. The inputs are the CXR images and corresponding lung and heart masks. These anatomy masks are derived from the segmentation network in a semi-supervised manner. The anatomy-aware attention modules operate on the upsampled feature spaces from dense block-3 and dense block-4, with the help of downsampled anatomy segmentation masks. The feature space calibrated with the supervision of anatomy knowledge from each of the anatomy-aware attention modules is pooled by the PWAP layers and concatenated. The final fully connected layer outputs pathology class scores by taking in these concatenated features as input.

where, $i \in \{1, \dots, C\}$. Finally, we get the background-suppressor attention vector by,

$$\mathbf{A}_{BkS} = \frac{\mathbf{A}_{LE} + \mathbf{A}_{HE}}{2} \quad (13)$$

Next, we denote the downsampled lung and heart masks, respectively, as $\mathbf{M}_{lung} \in \mathbb{R}^{H \times W \times 1}$ and $\mathbf{M}_{heart} \in \mathbb{R}^{H \times W \times 1}$. The shape of the feature map is \mathbf{F}_{DB}^{US} is $H \times W \times C$ while the shape of the masks, \mathbf{M}_{lung} , and \mathbf{M}_{heart} is $H \times W \times 1$. For consistent channel dimensions \mathbf{M}_{lung} , and \mathbf{M}_{heart} are broadcasted to the shape $H \times W \times C$. Afterward, we element-wise multiply the attention vectors, \mathbf{A}_{LE} with \mathbf{F}_{DB}^{US} and \mathbf{M}_{lung} , \mathbf{A}_{HE} with \mathbf{F}_{DB}^{US} and \mathbf{M}_{heart} , and \mathbf{A}_{BkS} with \mathbf{F}_{DB}^{US} to get three feature spaces, \mathbf{R}_{LE} , \mathbf{R}_{HE} , and \mathbf{R}_{BkS} , respectively.

$$\mathbf{R}_{LE} = \mathbf{A}_{LE} \odot \mathbf{M}_{lung} \odot \mathbf{F}_{DB}^{US} \quad (14)$$

$$\mathbf{R}_{HE} = \mathbf{A}_{HE} \odot \mathbf{M}_{heart} \odot \mathbf{F}_{DB}^{US} \quad (15)$$

$$\mathbf{R}_{BkS} = \mathbf{A}_{BkS} \odot \mathbf{F}_{DB}^{US} \quad (16)$$

where \odot represents the element-wise multiplication operation. Thus, we obtain two anatomy attentive feature space \mathbf{R}_{LE} , $\mathbf{R}_{HE} \in \mathbb{R}^{H \times W \times C}$, and the background suppressed feature space, $\mathbf{R}_{BkS} \in \mathbb{R}^{H \times W \times C}$. For faster convergence and

removal of any internal covariate shift among \mathbf{R}_{LE} , \mathbf{R}_{HE} , and \mathbf{R}_{BkS} , batch normalization operation is applied individually. Next, we sum all of the three feature spaces and apply batch normalization to obtain the final feature space $\mathbf{R} \in \mathbb{R}^{H \times W \times C}$ by,

$$\mathbf{R} = BN \left(BN(\mathbf{R}_{LE}) + BN(\mathbf{R}_{HE}) + BN(\mathbf{R}_{BkS}) \right) \quad (17)$$

Here, $BN(\cdot)$ denotes the batch normalization operation. Since \mathbf{A}_{LE} is multiplied by \mathbf{M}_{lung} and \mathbf{F}_{DB}^{US} , \mathbf{A}_{LE} provides attention to the spatial regions responsible for respiratory diseases. Similarly, \mathbf{A}_{HE} provides attention to heart-related (cardiac) diseases.

Probabilistic Weighted Average Pooling (PWAP) Module:

The traditional global average pooling or max-pooling layer provides the same weight to all spatial regions of the input. However, in many cases, the object of interest may reside in a salient region that is more important than others. Usually, a thoracic disease is often characterized by an anatomy region and lesion areas that constitute much smaller portions than the entire image. Thus, to further enhance the attention mechanism of our Anatomy-XNet, we have used a novel PWAP module (post-AAA) in conjunction with the AAA block and a PWAP

module (intra-AAA) within the AAA block. In this module, we learn the weight of each spatial position to guide Anatomy-XNet towards lesion localization during training through a 1×1 convolutional filter. The 1×1 convolutional filter has been chosen as we aim to learn the weight at a single spatial position; surrounding information is unwanted. First, we get the probability map $\mathbf{P} \in \mathbb{R}^{H \times W \times 1}$ from the input feature map $\mathbf{F}^{inp} \in \mathbb{R}^{H \times W \times C}$ by,

$$\mathbf{P}_{i,j,1} = \mathcal{S} \left(\sum_{c=1}^C \mathbf{K}_{1,1,c} * \mathbf{F}_{i,j,c}^{inp} \right), \quad i \in \{1, \dots, H\}, \quad j \in \{1, \dots, W\} \quad (18)$$

Here, $\mathcal{S}(\cdot)$ denotes the sigmoid function and \mathbf{K} is the learnable convolutional filter. Afterward, we broadcast the probability map \mathbf{P} to dimension of $H \times W \times C$ and elementwise multiply with the input feature map \mathbf{F}^{inp} to obtain the weighted feature space \mathbf{X} . Then we normalize the feature space \mathbf{X} and finally, obtain the pooled feature vector \mathbf{V} of size $1 \times 1 \times C$ by,

$$\mathbf{X}_{i,j,c} = \mathbf{F}_{i,j,c}^{inp} \odot \mathbf{P}_{i,j,c} \quad (19)$$

$$\mathbf{V}_{1,1,c} = \frac{\sum_{i=1}^H \sum_{j=1}^W \mathbf{X}_{i,j,c}}{\sum_{i=1}^H \sum_{j=1}^W \mathbf{P}_{i,j,c}} \quad (20)$$

Classifier:

Let $V_1 \in \mathbb{R}^{1 \times 1 \times C_1}$, $V_2 \in \mathbb{R}^{1 \times 1 \times C_2}$ be the pooled feature vectors from the PWAP modules (post-AAA) connected to the AAA modules that work on the third and fourth dense blocks, respectively. Here, $C_1 = 512$ and $C_2 = 1024$. We concatenate these pooled feature vectors together and pass them through a fully connected layer. The output $p(i|I)$ from this fully connected layer is then passed through a sigmoid layer and normalized by,

$$p_s(i|I) = \frac{1}{1 + \exp(-p(i|I))} \quad (21)$$

where I is a CXR image and $p_s(i|I)$ represents the probability score of I belonging to the i^{th} class, where $i \in \{1, 2, \dots, n\}$. n represents the number of pathologies.

Loss functions:

The pathological labels in each CXR of each of the dataset are expressed as an n -dimensional label vector, $L = [l_1, \dots, l_i, \dots, l_n]$ where $l_i \in \{0, 1\}$, and n represents the number of pathologies presented in each dataset. l_i represents whether there is any pathology, i.e., 1 for presence and 0 for absence. We optimize the weight parameters of our model by minimizing the binary cross entropy (BCE) loss defined as,

$$\mathcal{L}_{cls} = -\frac{1}{n} \sum_{i=1}^n \left[l_i \log(p_s(i|I)) + (1 - l_i) \log(1 - p_s(i|I)) \right] \quad (22)$$

where l_i is the ground-truth label of the i^{th} class and n is the number of pathologies.

IV. TRAINING

A. Datasets

NIH: The NIH chest X-ray dataset [5] consists of 112,120 X-rays from 30,805 unique patients with 14 diseases. We

strictly follow the official split of NIH, 70% for training, 10% for validation, and 20% for testing, for conducting experiments and fair comparison with previous works.

CheXpert: The CheXpert dataset [21] consists of 224,316 X-rays of 65,240 patients. The official specific validation and test datasets consist of 200, and 500 studies respectively and are annotated for five diseases: atelectasis, cardiomegaly, consolidation, edema, and pleural effusion. We use the “U-Ones” strategy from [21] for training and evaluating our model on the CheXpert dataset.

MIMIC-CXR: The MIMIC-CXR dataset [22] contains 377,111 X-rays with 14 diseases. We combine all non-positive labels (negative, not mentioned, and uncertain) into an aggregate negative label [40] for experimenting on this dataset.

JSRT: We use the JSRT [23] as annotated dataset to train the segmentation model. The segmentation annotations for JSRT, including heart and lung, are obtained from [46].

B. Training Scheme for Segmentation

We follow the procedure outlined in [24] for preprocessing and hyper-parameter settings to utilize the semi-supervised training pipeline. The segmentation module is based on U-Net architecture. We resize the CXR images to 256×256 . We run the training for 30 epochs with a batch size of 24. We set the initial learning rate 0.0001 and decay with a factor of 0.5 after every ten epochs. We utilize the large-scale datasets as the unannotated subset, i.e., for training the model on the NIH dataset, the NIH dataset is used as an unannotated subset. Thus, we get three separate segmentation models, where NIH, CheXpert, and MIMIC-CXR datasets are used as an unannotated subset, respectively. We use the JSRT dataset as the annotated subset in all three cases. Calculating accuracy in external datasets such as NIH, CheXpert, or MIMIC-CXR is impossible due to the unavailability of the ground truths for them. For this reason, the validation dataset for the semi-supervised setting in all three cases is comprised of only CXR images from the JSRT dataset. We choose the checkpoint with the highest dice score on this validation dataset as the final model. The selected models for NIH, CheXpert, and MIMIC-CXR datasets have achieved a validation dice score of 0.7437, 0.7395, and 0.7417, respectively. These models are used to generate anatomy masks for their corresponding datasets.

We binarize these segmentation results by following the procedure outlined in [24]. Let the final output from a segmentation model for a particular input CXR is $\mathbf{X} \in \mathbb{R}^{C \times H \times W}$, where H and W are respectively the height and width of the input CXR image, and C denotes the number of output channels. For our case, C is 3 where $C = 1, 2, 3$ represents “Background”, “Lung”, and “Heart” respectively. To generate the binarized lung mask $\mathbf{M}_{lung} \in \mathbb{R}^{H \times W}$ and heart mask $\mathbf{M}_{heart} \in \mathbb{R}^{H \times W}$, first, we apply the softmax operation across the channel axis of the \mathbf{X} to generate the probability scores of each channel at every spatial position. For at a particular spatial position of $\mathbf{X}_{c,i,j}$, if the lung channel achieves the maximum probability out of all channels, then the same spatial position at $(\mathbf{M}_{lung})_{i,j}$ is denoted as 1, otherwise 0. For binarizing the heart mask, if the heart channel achieves the

maximum probability out of all channels, then the same spatial position at $(\mathbf{M}_{\text{heart}})_{i,j}$ is denoted as 1, otherwise 0.

C. Training Scheme for Classification

We initialize all the backbone weights with DenseNet-121 pre-trained on ImageNet. In terms of image size, for a fair comparison with others, we follow [13], [15], [17], [43] and resize the CXR images to 256×256 , and then randomly crop 224×224 patches as inputs [16]. However, 224×224 is too small to predict small and subtle diseases like nodules, pneumonia in CXR. For that reason, we train our model on a larger image size as well. To utilize the larger input image dimension, we resize the CXR images to 586×586 , and then randomly crop 512×512 patches as inputs. We normalize the input images with the mean and standard deviation of the ImageNet training set. We follow [16] and take advantage of flipping to increase the variation and the diversity of training samples. For validation and inference, we use a centrally cropped sub-image of 512×512 for 586×586 and 224×224 for 256×256 dimensions as input. For a fairer comparison, we follow [16], [42], and take advantage of horizontal flipping and cropping at five different positions to augment the test data and using average probabilities of ten cropped sub-images (four corner crops and one central crop plus horizontally flipper version of these) as the final prediction. The anatomy masks from the segmentation network are resized to 84×84 before passing to the AAA modules. We use Adam optimizer with standard parameters ($\beta_1 = 0.9$ and $\beta_2 = 0.99$). The batch size is set to 60 with a gradient accumulation step of 2. We set the initial learning rate 0.0001 and run the training for 20 epochs. Following previous studies, [5], [42], we employ the percentage area under the receiver operating characteristic curve (AUC) for performance evaluation and choose the model with the highest validation AUC for evaluation on the test dataset.

V. EXPERIMENTAL RESULTS AND ANALYSIS

A. Performance on NIH-dataset

We compare our proposed Anatomy-XNet with previously published state-of-the-art methods including: Deep Convolutional Neural Network (DCNN) [5], deep network with long-short-term-memory unit (LSTM-Net) [32], TextImage Embedding network (TieNet) [35], Attention-Guided Curriculum Learning (AGCL) [10], the method presented by Ho *et al.* [36], Segmentation-Based Deep Fusion Network (SDFN) [19], Category-wise Residual Attention Learning (CRAL) [12], CheXNet [15], DualCheXNet [37], Lesion Location Attention Guided Network (LLAGNet) [11], the methods of Wan *et al.* [13], Yan *et al.* [16], Luo *et al.* [42], Daniel *et al.* [20], Keidar *et al.* [18], and MANet [17]. We have implemented the methods of Daniel *et al.* [20], Keidar *et al.* [18], and MANet [17], and evaluated their performance on the official test data split of the NIH dataset with input image dimension of 224×224 . For the methods of Ho *et al.* [36] and DualCheXNet [37], results have been reported from their implementations. The results for the rest of the methods are quoted from [42].

As shown in Table II, the method proposed by Luo *et al.* [42] is the previous state-of-the-art yielding an AUC of 83.49%, while our proposed Anatomy-XNet exceeds all the compared models and achieves a new state-of-the-art performance of 84.79% AUC. With a higher input image dimension of 512×512 , our proposed framework boosts performance to an AUC score of 85.66%. Specifically, our classification results outperform others in 10 out of 14 categories. Our model achieves a slightly worse but competitive score for the rest of the pathologies.

B. Performance on CheXpert-dataset

The results on CheXpert are compared in Table III. Most methods exploit ensembles of multiple models to pursue higher scores. For example, an ensemble of 30 generated checkpoints of DenseNet-121 [21] achieves a mean AUC of 89.30%. In this paper, we focus on comparing the results achieved by single models. We quote the single model performance for Pham *et al.* [43], and Allaouzi *et al.* [41] from their implementations. We report the ensemble result of Irvin *et al.* [21] as single model performance is not given in their paper. To compare with approaches that have utilized segmentation masks, we have implemented the methods of Daniel *et al.* [20], Keidar *et al.* [18], and MANet [17], and evaluated their performance on the official validation split with input image dimension of 224×224 . The results from Table III show that our model achieved an AUC of 90.77% and 91.13% with input image dimensions of 224×224 and 512×512 , respectively, surpassing the previous state of the art results. We have also submitted our single Anatomy-XNet model with DenseNet-121 as the backbone for the online evaluation on the Stanford CheXpert leaderboard. With input size of 224×224 , our single Anatomy-XNet has scored an AUC score of 91.10% and 2.2 radiologists under the curve, achieving a very competitive score compared to the other single models.

C. Performance on MIMIC-CXR-dataset

We compare our proposed Anatomy-XNet with previously published state-of-the-art methods including: Densenet-KG [39], VSE-GCN [38], the method of Keidar *et al.* [18], MANet [17], the method of Daniel *et al.* [20], and CheXclusion [40]. For data split, we follow the data split outlined in [40]¹. The results of Densenet-KG [39], VSE-GCN [38] have been quoted from the implementation of VSE-GCN [38]. We report the result of CheXclusion [40] from their implementation. We have implemented the methods of Daniel *et al.* [20], Keidar *et al.* [18], and MANet [17], and evaluated their performance on the test data split with input image dimension of 224×224 . The results are shown in Table IV. Our proposed model with both input image dimensions of 224×224 and 512×512 has achieved higher performance than the compared models. In [40], the authors have used an ensemble of five different checkpoints initialized with different random seeds. For fair comparison, we follow the same procedure and generate an ensemble score of five Anatomy-XNet initiated with different

¹<https://github.com/LalehSeyyed/CheXclusion>

TABLE II: PATHOLOGY-WISE PERFORMANCE COMPARISON OF THE PROPOSED METHOD WITH STATE-OF-THE-ART SYSTEMS ON THE NIH DATASET*. THE TWO BEST RESULTS ARE SHOWN IN RED AND BLUE.

Method	Emph	Fibr	Hern	Infi	PT	Mass	Nodu	Atel	Card	Cons	Edem	Effu	Pne1	Pne2	Average
Methods without Utilizing Segmentation Masks															
DCNN [5]	81.50	76.90	76.70	60.90	70.80	70.60	67.10	71.60	80.70	70.80	83.50	78.40	63.30	80.60	73.81
LSTM-Net [32]	84.20	75.70	82.40	67.50	72.40	72.70	77.80	73.30	85.80	71.70	80.60	80.60	69.00	80.50	76.73
TieNet [35]	86.50	79.60	87.60	66.60	73.50	72.50	68.50	73.20	84.40	70.10	82.90	79.30	72.00	84.70	77.24
AGCL [10]	90.75	81.79	87.47	68.92	76.47	81.36	75.45	75.57	88.65	72.83	84.75	81.91	72.92	84.99	80.27
Ho <i>et al.</i> [36]	87.50	75.60	83.60	70.30	77.40	83.50	71.60	79.50	88.70	78.60	89.20	87.50	74.20	86.30	80.97
CRAL [12]	90.80	83.00	91.70	70.20	77.80	83.40	77.30	78.10	88.00	75.40	85.00	82.90	72.90	85.70	81.59
CheXNet [15]	92.49	82.19	93.23	68.94	79.25	83.07	78.14	77.95	88.16	75.42	84.96	82.68	73.54	85.13	81.80
DualCheXNet [37]	94.20	83.70	91.20	70.50	79.60	83.80	79.60	78.40	88.80	74.60	85.20	83.10	72.70	87.60	82.30
LLAGNet [11]	93.90	83.20	91.60	70.30	79.80	84.10	79.00	78.30	88.50	75.40	85.10	83.40	72.90	87.70	82.37
Wang <i>et al.</i> [13]	93.30	83.80	93.80	71.00	79.10	83.40	77.70	77.90	89.50	75.90	85.50	83.60	73.70	87.80	82.60
Yan <i>et al.</i> [16]	94.22	83.26	93.41	70.95	80.83	84.70	81.05	79.24	88.14	75.98	84.70	84.15	73.97	87.59	83.02
Luo <i>et al.</i> [42]	93.96	83.81	93.71	71.84	80.36	83.76	79.85	78.91	90.69	76.81	86.10	84.18	74.19	90.63	83.49
Methods Utilizing Segmentation Masks															
Daniel <i>et al.</i> [20]	84.34	80.97	81.24	69.80	76.34	82.42	76.55	81.06	90.59	80.10	88.05	86.50	75.17	84.80	81.28
SDFN [19]	92.10	83.50	91.10	70.00	79.10	81.50	76.50	78.10	88.50	74.30	84.20	83.20	71.90	86.60	81.50
Keidar <i>et al.</i> [18]	90.87	81.47	91.80	70.60	78.02	83.93	77.07	80.64	90.88	80.43	89.20	86.94	76.53	85.54	83.14
MANet [17]	88.41	82.35	91.70	70.34	78.24	85.42	79.09	82.12	90.53	80.91	88.38	87.19	77.30	86.66	83.47
Anatomy X-Net (224)	93.26	84.24	94.79	71.70	80.03	85.52	79.75	82.50	91.30	80.77	90.13	88.52	76.27	88.35	84.79
Anatomy X-Net (512)	94.91	86.87	94.28	71.77	79.42	86.70	83.69	83.16	91.21	81.04	90.23	88.95	77.04	90.05	85.66

* The 14 findings for NIH datasets are Emphysema (Emph), Fibrosis (Fibr), Hernia (Hern), Infiltration (Infi), Pleural Thickening (PT), Mass, Nodule (Nodu), Atelectasis (Atel), Cardiomegaly (Card), Consolidation (Cons), Edema (Edem), Effusion (Effu), Pneumonia (Pne1), and Pneumothorax (Pne2).

TABLE III: PATHOLOGY-WISE PERFORMANCE COMPARISON OF THE PROPOSED METHOD WITH STATE-OF-THE-ART SYSTEMS ON THE CHEXPERT DATASET. THE TWO BEST RESULTS ARE SHOWN IN RED AND BLUE.

Method	Atelectasis	Cardiomegaly	Edema	Consolidation	Pleural Effusion	Average
Methods without Utilizing Segmentation Masks						
Allaouzi <i>et al.</i> [41] LP	72.00	87.00	87.00	77.00	90.00	82.60
Allaouzi <i>et al.</i> [41] BR	72.00	88.00	87.00	77.00	90.00	82.80
Allaouzi <i>et al.</i> [41] CC	70.00	87.00	86.00	74.00	90.00	81.40
Irvin <i>et al.</i> [21] U-Zeros	81.10	84.00	92.90	93.20	93.10	88.80
Irvin <i>et al.</i> [21] U-Ones	85.80	83.20	94.10	89.90	93.40	89.30
Pham <i>et al.</i> [43] U-Zeros+CT+LSR	80.60	83.30	93.30	92.90	92.10	88.40
Pham <i>et al.</i> [43] U-Ones+CT+LSR	82.50	85.50	93.00	93.70	92.30	89.40
Methods Utilizing Segmentation Masks						
Daniel <i>et al.</i> [20]	84.83	80.93	94.60	87.96	93.22	88.30
Keidar <i>et al.</i> [18]	83.89	83.28	94.40	87.34	92.69	88.32
MANet [17]	84.99	84.90	94.69	88.24	92.70	89.10
Anatomy-XNet (224)	87.57	86.34	95.54	89.92	94.46	90.77
Anatomy-XNet (512)	88.61	86.13	95.73	90.94	94.23	91.13

TABLE IV: PATHOLOGY-WISE PERFORMANCE COMPARISON OF THE PROPOSED METHOD WITH STATE-OF-THE-ART SYSTEMS ON THE MIMIC-CXR DATASET[†]. THE TWO BEST RESULTS ARE SHOWN IN RED AND BLUE.

Method	Atel	Card	Cons	Edem	E.C.	Frac	L.L.	L.O.	N.F.	Effu	P.O.	Pne1	Pne2	S.D.	Average
Methods without Utilizing Segmentation Masks															
Densenet-KG [39]	69.40	74.60	64.00	79.00	65.10	60.50	57.40	60.90	77.80	80.90	65.00	57.20	68.90	78.10	68.50
VSE-GCN [38]	72.20	73.00	72.80	79.90	76.70	56.00	62.30	65.40	81.70	86.30	65.30	58.80	79.70	78.90	72.10
Chexclusion [40] **	83.70	82.80	84.40	90.40	75.70	71.80	77.20	78.20	86.80	93.30	84.80	74.80	90.30	92.70	83.40
Methods Utilizing Segmentation Masks															
Daniel <i>et al.</i> [20]	83.11	82.07	83.48	90.37	74.23	69.65	75.70	77.50	86.02	91.79	83.41	73.43	89.21	90.68	82.19
MANet [17]	83.20	81.97	84.04	90.24	73.93	70.89	76.50	77.81	86.31	92.17	85.24	74.07	89.26	91.63	82.66
Keidar <i>et al.</i> [18]	83.24	82.59	84.19	90.40	74.71	71.33	76.66	77.67	86.39	92.93	84.18	74.51	89.70	92.05	82.90
Anatomy X-Net (224)	83.80	82.63	85.21	90.82	75.47	74.26	77.11	78.76	86.95	93.32	86.51	75.95	90.90	92.71	83.88
Anatomy X-Net (512)	83.93	82.59	84.84	90.76	75.12	74.95	78.78	78.90	86.97	93.43	86.21	75.81	91.20	93.12	84.04

† The 14 pathologies for the MIMIC-CXR datasets are Atelectasis (Atel), Cardiomegaly (Card), Consolidation (Cons), Edema (Edem), Enlarged Cardiomediastinum (E.C.), Fracture (Frac), Lung Lesion (L.L.), Lung Opacity (L.O.), No Finding (N.F.), Pleural Effusion (Effu), Pleural Other (P.O.), Pneumonia (Pne1), Pneumothorax (Pne2), Support Devices (S.D.).

** Indicates that the result is obtained by the ensemble of 5 checkpoints.

random states. This ensemble on 224×224 input dimension has achieved an AUC of 84.43%, increasing the benchmark set by the proposed framework even higher.

D. Qualitative Visualization and Analysis

We produce the attention heatmaps to visualize the most indicative pathology areas on CXRs from the test dataset, interpreting the representational power of Anatomy-XNet. We generate these heatmaps using Gradient-weighted Class

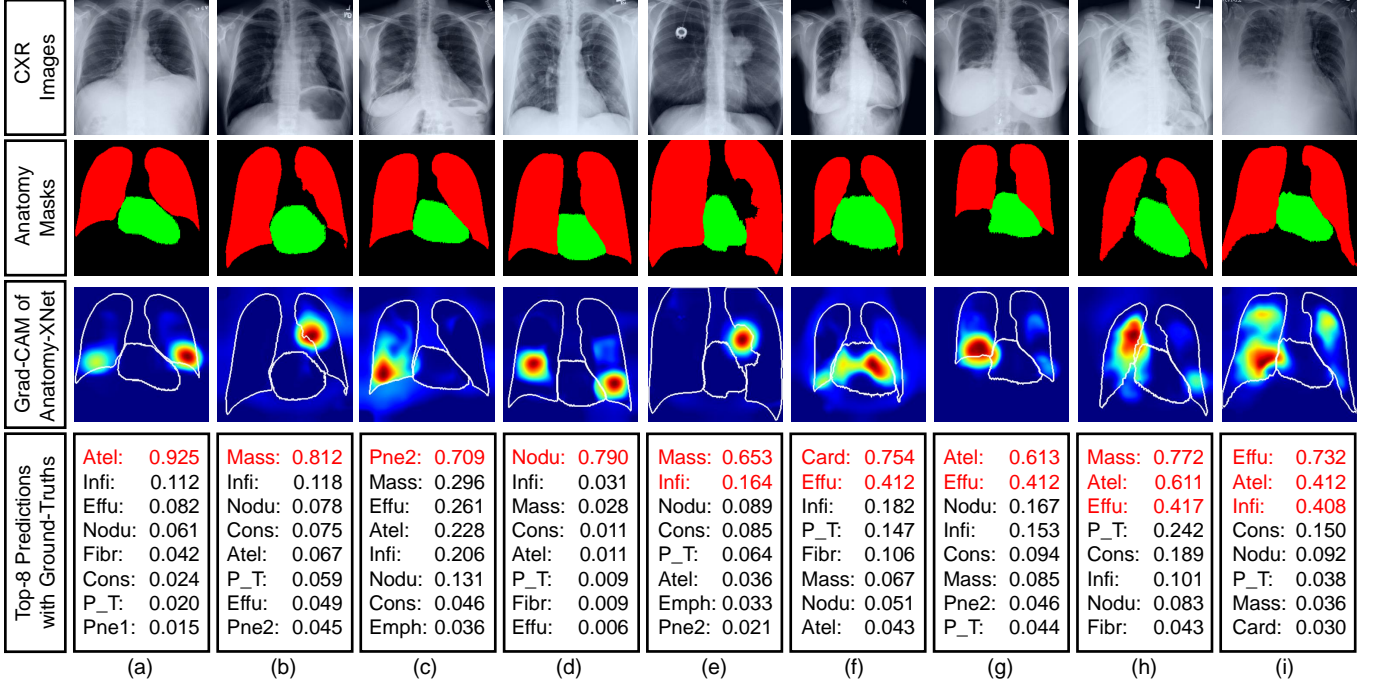


Fig. 4: Qualitative visualization of the Anatomy-XNet’s output on the NIH test dataset. The first and second rows depict the CXR images and their corresponding predicted anatomy masks, respectively. The third row shows the Grad-CAM of the Anatomy-XNet for the target classes. The contours of the anatomy segmentation masks are marked with white color on top of the heatmaps. The final row shows top-8 predicted findings and their corresponding prediction scores. The ground truth labels are highlighted in red color.

Activation Mappings (Grad-CAMs) [47]. Grad-CAMs use the gradients of any target class flowing into any convolutional layer to produce a low-resolution heatmap highlighting the important portions of the feature map activations of that layer that are responsible for detecting the target class. We construct the heatmaps for any target class by using the gradients of the feature map activations of the intended layer for that target class as the weights and performing a weighted sum of these feature map activations using those weights. The classifier layer of the proposed Anatomy-XNet works on the high-level feature vectors from both AAA modules, which are connected to the DB-3 and DB-4. To explore the proposed modules’ effectiveness qualitatively, we utilize the AAA modules’ output (fine-grained) as the feature map activations. We upscale these resulting heatmaps to the original image’s dimensions. For multilabel images, we superimpose the heatmaps for target classes on top of each other to get the final heatmap for that particular CXR image. These attention heatmaps, along with the CXR images, anatomy segmentation masks, and classification results, are shown in Fig. 4. A visual evaluation of the Grad-CAMs confirms the module’s anatomy awareness. Thus, similar to the process followed by a radiologist, the AAA module integrates the anatomy information responsible for a particular pathology within the model. In cases of imperfect mask segmentation (due to semi-supervised training setting), our proposed method still manages to capture the pathology relevant areas and give attention to them. Column (e) of Fig. 4 demonstrates

an example where the lung mask fails to contain the mass area. Nevertheless, our model localizes its attention in that area, demonstrating the efficacy of the proposed architecture’s resilience towards imperfect mask segmentation.

E. Effectiveness of AAA Modules

AAA modules are the driving blocks of our method that help the model learn the salient anatomy information associated with a particular thoracic disease. Our experiments find that classification performance improves from the baseline when we cascade a AAA module with a dense block. The baseline denotes the backbone model, DenseNet-121, without any integrated AAA modules. However, adding an AAA module with all the dense blocks does not enhance the performance. Because low-level spatial features from dense block-1 and dense block-2 might have outlier information which deteriorates the model performance by causing the model to give attention to noisy information. Again, applying AAA only on the highest level of features, in our case dense block-4, does not guarantee the best performance. Because due to subsequent pooling in these dense blocks, some important information may be lost in the later dense blocks presented in the previous blocks. To evaluate the efficacy of this effect, we have tested different levels of anatomy-aware attention on the NIH, MIMIC-CXR, and CheXpert datasets. First, we use an AAA module with dense block-4. This experiment is denoted by anatomy aware attention level-1 (AAA-L1). Afterward, we use one AAA module with dense block-4 and another with dense block-3.

TABLE V: INVESTIGATION OF THE CLASSIFICATION PERFORMANCE IN THE NIH, MIMIC-CXR (MIMIC), AND CHEXPERT (CXP) DATASETS⁸ WITH DIFFERENT SETTINGS. THE BEST RESULT IS SHOWN IN RED.

		Part 1: Investigation of the effectiveness of AAA modules.																					
Dataset	Method	Atel	Card	Effu	Infi	Mass	Nodu	Pne1	Pne2	Cons	Edem	Emph	Fibr	PT	Hern	N.F.	E.C.	Frac	L.L.	L.O.	P.O.	S.D.	Mean
NIH	Baseline	81.42	87.91	87.69	69.95	83.42	77.16	75.22	86.84	79.65	88.63	90.39	81.26	77.46	87.11	77.68	-	-	-	-	-	82.44	
	AAA-L1	82.27	91.06	88.51	71.04	85.24	79.29	76.98	87.16	80.67	89.59	92.41	83.41	78.82	93.39	78.68	-	-	-	-	-	84.27	
	AAA-L2	82.50	91.30	88.52	71.70	85.52	79.75	76.27	88.35	80.77	90.13	93.26	84.24	80.04	94.78	78.72	-	-	-	-	-	84.79	
	AAA-L3	82.20	91.18	88.12	71.34	84.88	78.95	76.16	87.80	80.52	89.60	92.79	84.14	79.02	92.85	78.58	-	-	-	-	-	84.25	
MIMIC	Baseline	82.15	81.57	91.77	-	-	-	74.87	88.59	83.49	89.60	-	-	-	-	87.00	74.56	72.54	78.22	78.08	84.61	91.62	82.76
	AAA-L1	83.84	82.99	93.37	-	-	-	75.93	90.97	85.08	90.70	-	-	-	-	86.98	75.42	73.07	77.34	78.78	84.89	92.78	83.72
	AAA-L2	83.80	82.63	93.32	-	-	-	75.95	90.90	85.21	90.82	-	-	-	-	86.95	75.47	74.26	77.11	78.76	86.51	92.70	83.88
	AAA-L3	83.73	82.97	93.36	-	-	-	75.87	90.81	84.83	90.74	-	-	-	-	86.94	75.64	73.05	76.55	78.79	85.41	92.72	83.67
CXP	Baseline	83.03	81.23	93.01	-	-	-	-	87.93	93.89	-	-	-	-	-	86.98	-	-	-	-	-	-	87.82
	AAA-L1	87.01	85.73	93.78	-	-	-	-	88.75	94.67	-	-	-	-	-	88.56	-	-	-	-	-	-	89.99
	AAA-L2	87.57	86.34	94.46	-	-	-	-	89.92	95.54	-	-	-	-	-	89.10	-	-	-	-	-	-	90.77
	AAA-L3	86.63	85.47	93.39	-	-	-	-	88.21	94.02	-	-	-	-	-	89.38	-	-	-	-	-	-	89.54
Part 2: Investigation of the effectiveness of PWAP modules.																							
Dataset	Pool type	Atel	Card	Effu	Infi	Mass	Nodu	Pne1	Pne2	Cons	Edem	Emph	Fibr	PT	Hern	N.F.	E.C.	Frac	L.L.	L.O.	P.O.	S.D.	Mean
NIH	PWAP	82.50	91.30	88.52	71.70	85.52	79.75	76.27	88.35	80.77	90.13	93.26	84.24	80.04	94.78	78.72	-	-	-	-	-	-	84.79
	Gem	82.39	91.51	88.31	70.84	84.45	79.46	76.86	88.11	80.38	89.99	93.18	83.44	79.15	94.53	78.55	-	-	-	-	-	-	84.47
	Average	82.34	91.11	88.56	71.35	85.28	79.49	76.47	88.21	80.60	89.90	92.01	84.05	79.90	93.15	78.62	-	-	-	-	-	-	84.46
	Max	82.05	91.24	88.30	70.90	84.50	78.72	77.14	87.05	81.05	89.76	92.56	83.17	78.05	93.35	78.66	-	-	-	-	-	-	84.13
MIMIC	PWAP	83.80	82.63	93.32	-	-	-	75.95	90.90	85.21	90.82	-	-	-	-	86.95	75.47	74.26	77.11	78.76	86.51	92.70	83.88
	Gem	83.71	82.84	93.40	-	-	-	75.47	91.05	84.94	90.59	-	-	-	-	86.91	75.08	73.40	77.51	78.59	85.13	92.84	83.68
	Average	83.68	82.81	93.28	-	-	-	75.41	90.23	84.63	90.49	-	-	-	-	86.92	75.13	72.98	76.29	78.46	85.47	92.74	83.46
	Max	83.50	82.76	93.25	-	-	-	75.22	90.72	84.47	90.51	-	-	-	-	86.84	74.36	72.27	77.22	78.50	84.18	92.70	83.32
CXP	PWAP	87.57	86.34	94.46	-	-	-	-	89.92	95.54	-	-	-	-	-	89.10	-	-	-	-	-	-	90.77
	Gem	85.23	85.47	93.65	-	-	-	-	88.93	92.76	-	-	-	-	-	86.11	-	-	-	-	-	-	89.21
	Average	86.94	84.89	93.19	-	-	-	-	89.10	94.27	-	-	-	-	-	88.14	-	-	-	-	-	-	89.68
	Max	84.90	81.44	93.77	-	-	-	-	87.16	94.04	-	-	-	-	-	87.77	-	-	-	-	-	-	88.26
Part 3: Investigation of different anatomy mask sizes.																							
Dataset	Mask size	Atel	Card	Effu	Infi	Mass	Nodu	Pne1	Pne2	Cons	Edem	Emph	Fibr	PT	Hern	N.F.	E.C.	Frac	L.L.	L.O.	P.O.	S.D.	Mean
NIH	28 × 28	82.18	90.88	88.51	71.69	84.94	79.87	76.32	88.02	80.84	89.84	93.02	84.27	78.97	94.33	78.76	-	-	-	-	-	-	84.55
	56 × 56	82.33	91.57	88.41	71.76	85.64	78.60	76.97	88.02	80.96	89.66	92.93	84.01	79.22	94.84	78.65	-	-	-	-	-	-	84.64
	84 × 84	82.50	91.30	88.52	71.70	85.52	79.75	76.27	88.35	80.77	90.13	93.26	84.24	94.78	78.72	-	-	-	-	-	-	-	84.79
	28 × 28	83.59	82.83	93.26	-	-	-	75.39	90.44	84.50	90.55	-	-	-	-	86.84	75.28	72.19	76.68	78.34	84.76	92.69	83.38
MIMIC	56 × 56	83.64	82.90	93.34	-	-	-	75.58	90.55	84.98	90.59	-	-	-	-	86.85	75.09	73.96	77.56	78.48	85.37	92.61	83.68
	84 × 84	83.80	82.63	93.32	-	-	-	75.95	90.90	85.21	90.82	-	-	-	-	86.95	75.47	74.26	77.11	78.76	86.51	92.70	83.88
	28 × 28	86.98	86.09	93.77	-	-	-	-	89.03	94.76	-	-	-	-	-	88.21	-	-	-	-	-	-	90.13
	56 × 56	87.16	86.40	94.10	-	-	-	-	89.51	95.10	-	-	-	-	-	88.75	-	-	-	-	-	-	90.45
CXP	28 × 28	87.57	86.34	94.46	-	-	-	-	89.92	95.54	-	-	-	-	-	89.10	-	-	-	-	-	-	90.77
	384 × 384	83.02	90.13	88.86	71.91	85.56	81.51	77.64	90.15	80.65	89.45	94.24	85.48	79.33	92.86	78.91	-	-	-	-	-	-	85.06
	512 × 512	83.16	91.21	88.95	71.77	86.70	83.69	77.04	90.05	81.04	90.23	94.91	86.87	79.42	94.28	79.09	-	-	-	-	-	-	85.66
	224 × 224	83.80	82.63	93.32	-	-	-	75.95	90.90	85.21	90.82	-	-	-	-	86.95	75.47	74.26	77.11	78.76	86.51	92.70	83.88
MIMIC	384 × 384	83.50	82.80	93.33	-	-	-	75.96	91.26	84.91	90.67	-	-	-	-	87.01	74.70	74.50	79.21	78.73	86.05	93.00	83.97
	512 × 512	83.93	82.59	93.43	-	-	-	75.81	91.20	84.84	90.76	-	-	-	-	86.97	75.12	74.95	78.78	78.90	86.21	93.12	84.04
	224 × 224	87.57	86.34	94.46	-	-	-	-	89.92	95.54	-	-	-	-	-	89.10	-	-	-	-	-	-	90.77
	384 × 384	88.35	86.43	94.29	-	-	-	-	90.35	95.38	-	-	-	-	-	89.14	-	-	-	-	-	-	90.96
CXP	512 × 512	88.61	86.13	94.23	-	-	-	-	90.94	95.73	-	-	-	-	-	89.27	-	-	-	-	-	-	91.13

⁸ The 21 findings across all three datasets are Atelectasis (Atel), Cardiomegaly (Card), Pleural Effusion (Effu), Infiltration (Infi), Mass, Nodule (Nodu), Pneumonia (Pne1), Pneumothorax (Pne2), Consolidation (Cons), Edema (Edem), Emphysema (Emph), Fibrosis (Fibr), Pleural Thickening (PT), Hernia (Hern), No Finding (N.F.), Enlarged Cardiomediastinum (E.C.), Fracture (Frac), Lung Lesion (L.L.), Lung Opacity (L.O.), Pleural Other (P.O.), Support Devices (S.D.).

F. Effectiveness of PWAP Modules

To demonstrate the effectiveness of PWAP modules, we replace all the PWAP layers in Anatomy-XNet with average pooling, max pooling, and generalized mean pooling [48], respectively, and run the experiment while keeping all the other hyperparameters the same. The results across all the datasets, shown in part-2 of Table V, depict the effectiveness of the proposed module. In Fig. 5, the Grad-CAMs of the feature spaces, before and after passing through the PWAP layer (intra-AAA) inside the AAA module connected with the fourth dense block, are shown. The heatmaps are resized to the CXR images' dimension and overlaid on the images. The

PWAP module tweaks the feature space to focus on the lesion areas more prominently by removing unwanted attention.

G. Effect of Anatomy Mask Dimension

Incorporating anatomy masks at their original resolution in high-level feature space maps encoded by dense blocks is computationally highly intensive. Due to hardware constraints, the feature spaces are upsampled while masks are downsampled to an intermediate shape. To demonstrate the effect of dimension of anatomy masks, we vary the intermediate dimensions of the anatomy masks and evaluate the performances of Anatomy-XNet. Part-3 of Table V presents performance numbers across all datasets. Here, we observe that the performance of Anatomy-XNet improves as we increase the dimension of the anatomy masks. This implies that, with the larger intermediate dimensions of anatomy masks, we can possibly further improve the performance of Anatomy-XNet.

H. Effect of Different Input Image Sizes

We perform experiments to investigate the effect of varying input image dimensions on classification performance. We

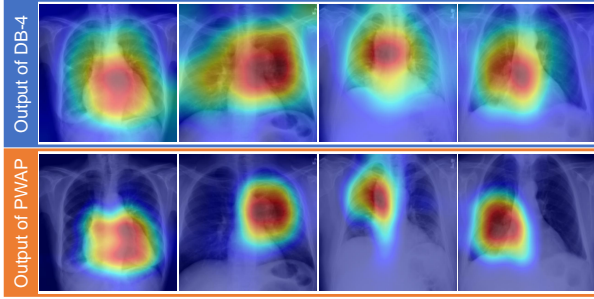


Fig. 5: Demonstration of feature space recalibration performed by the PWAP module. The first row depicts the feature space derived from the DB-4 block. The second row shows the recalibrated feature space by the PWAP module (intra-AAA) of the AAA module connected to DB-4.

resize the CXR images into three different sizes: 256×256 , 438×438 , and 586×586 and crop patches of 224×224 for 256×256 , 384×384 for 438×438 , and 512×512 for 586×586 to use as input images. The classification performances on all three datasets for different input sizes are given in the part-4 of Table V. The classification results show that enlarging the input image size increases the average AUC. More specifically, we observe that the increase for small lesions such as nodules is significant. However, increasing the image dimension for large lesions, such as cardiomegaly, are not beneficial.

I. Investigation of the Impact of Imperfect Segmentation

To simulate the resilience of the proposed Anatomy-XNet towards imperfect segmentation masks, we randomly apply cutout operations [49] on the predicted anatomy segmentation regions with different window sizes and measure the AUC score. We perform the cutout operation three times for each window size, measure AUC each time, and take the average as the final AUC score for that particular cutout window. We use cutout windows of sizes 16×16 , 24×24 , 32×32 , 40×40 , 48×48 , 56×56 , 64×64 , 72×72 , and 80×80 . Next, we apply the exact same cutout operations at exactly the same locations of the anatomy masks and use them to evaluate the AUC of segmentation mask-based approaches [17], [18], [20] and compare their drop in classification performance with our method. The AUC scores against different cutout window sizes are shown in Fig. 6. The proposed Anatomy-XNet shows only around 0.34% performance degradation against cutout operations and maintains stable performance against increasing window sizes. On the other hand, the methods of Keidar *et al.* [18], Daniel *et al.* [20], and MANet [17] show a larger degradation in classification performance, around 2 – 4%, against increasing cutout window size.

VI. CONCLUSION

In this paper, we propose a semi-supervised anatomy-aware convolutional neural network for thoracic disease classification named the Anatomy-XNet. Departing from the previous works that rely on the chest X-ray image only or attention mechanisms guided by the model prediction, the proposed network

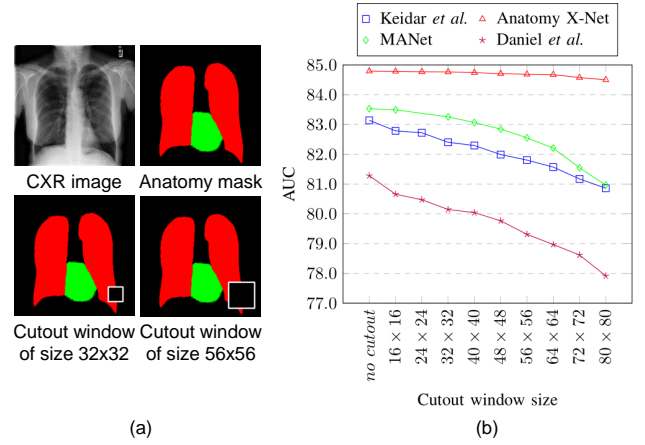


Fig. 6: (a) Visualization of cutout window of two different sizes. The first row shows the CXR image and its corresponding anatomy masks. The red color represents the lung mask, and the green color represents the heart mask. The second row demonstrates two different cutout windows of 32×32 and 56×56 dimensions, plotted with the white contour. (b) Simulation of classification performance drop against increasing imperfection in segmentation masks.

is guided by prior anatomy segmentation information to act similar to a radiologist by focusing on relevant anatomical regions associated with the thoracic disease. Extensive experiments demonstrate that combining our novel AAA and PWAP modules within a backbone Densenet-121 model in a unified framework yields state-of-the-art performance on the NIH chest X-ray dataset. The Anatomy-XNet achieves an average AUC score of 85.66% on the official NIH test set, surpassing the former best performing method published on this dataset. The proposed method also reaches an AUC of 91.13% on the official validation split of the Stanford CheXpert dataset, and 84.04% on the MIMIC-CXR dataset, achieving state-of-the-art performance on these two datasets as well.

REFERENCES

- [1] S. Raoof, D. Feigin, A. Sung, S. Raoof, L. Irugulpati, and E. C. Rosenow III, "Interpretation of plain chest roentgenogram," *Chest*, vol. 141, no. 2, pp. 545–558, 2012.
- [2] P. Yu, H. Xu, Y. Zhu, C. Yang, X. Sun, and J. Zhao, "An automatic computer-aided detection scheme for pneumoconiosis on digital chest radiographs," *J. Digit. Imaging*, vol. 24, no. 3, pp. 382–393, 2011.
- [3] S. Jaeger, A. Karargyris, S. Candemir, L. Folio, J. Siegelman, F. Callaghan, Z. Xue, K. Palaniappan, R. K. Singh, S. Antani *et al.*, "Automatic tuberculosis screening using chest radiographs," *IEEE Trans. Med. Imag.*, vol. 33, no. 2, pp. 233–245, 2013.
- [4] G. Litjens, T. Kooi, B. E. Bejnordi, A. A. A. Setio, F. Ciompi, M. Ghafoorian, J. A. Van Der Laak, B. Van Ginneken, and C. I. Sánchez, "A survey on deep learning in medical image analysis," *Med. Image Anal.*, vol. 42, pp. 60–88, 2017.
- [5] X. Wang, Y. Peng, L. Lu, Z. Lu, M. Bagheri, and R. M. Summers, "Chestx-ray8: Hospital-scale chest x-ray database and benchmarks on weakly-supervised classification and localization of common thorax diseases," in *Proc. IEEE CVPR*, 2017, pp. 3462–3471.
- [6] J. Deng, W. Dong, R. Socher, L. Li, Kai Li, and Li Fei-Fei, "Imagenet: A large-scale hierarchical image database," in *IEEE CVPR*, 2009, pp. 248–255.
- [7] S. Liu and W. Deng, "Very deep convolutional neural network based image classification using small training sample size," in *ACPR*, 2015, pp. 730–734.

[8] C. Szegedy, Wei Liu, Yangqing Jia, P. Sermanet, S. Reed, D. Anguelov, D. Erhan, V. Vanhoucke, and A. Rabinovich, "Going deeper with convolutions," in *IEEE CVPR*, 2015, pp. 1–9.

[9] K. He, X. Zhang, S. Ren, and J. Sun, "Deep residual learning for image recognition," in *IEEE CVPR*, 2016, pp. 770–778.

[10] Y. Tang, X. Wang, A. P. Harrison, L. Lu, J. Xiao, and R. Summers, "Attention-guided curriculum learning for weakly supervised classification and localization of thoracic diseases on chest radiographs," in *MLMI@MICCAI*, 2018.

[11] B. Chen, J. Li, G. Lu, and D. Zhang, "Lesion location attention guided network for multi-label thoracic disease classification in chest x-rays," *IEEE J. of Biomed. and Health Inform.*, pp. 2016–2027, 2020.

[12] Q. Guan and Y. Huang, "Multi-label chest x-ray image classification via category-wise residual attention learning," *Pattern Recognit. Letters*, vol. 130, pp. 259–266, 2020.

[13] H. Wang, S. Wang, Z. Qin, Y. Zhang, R. Li, and Y. Xia, "Triple attention learning for classification of 14 thoracic diseases using chest radiography," *Med. Image Anal.*, vol. 67, p. 101846, 2020.

[14] C. Clarke and A. Dux, *Chest X-rays for medical students*. John Wiley & Sons, 2017.

[15] P. Rajpurkar, J. Irvin, K. Zhu, B. Yang, H. Mehta, T. Duan, D. Ding, A. Bagul, C. Langlotz, K. Shpanskaya, M. Lungren, and A. Ng, "CheXnet: Radiologist-level pneumonia detection on chest x-rays with deep learning," *ArXiv*, vol. abs/1711.05225, 2017.

[16] C. Yan, J. Yao, R. Li, Z. Xu, and J. Huang, "Weakly supervised deep learning for thoracic disease classification and localization on chest x-rays," in *Proc. ACM Int. Conf. on Bioinformatics, Computational Biology, and Health Informatics*, 2018.

[17] Y. Xu, H.-K. Lam, and G. Jia, "Manet: A two-stage deep learning method for classification of covid-19 from chest x-ray images," *Neurocomputing*, vol. 443, pp. 96–105, 2021.

[18] D. Keidar, D. Yaron, E. Goldstein, Y. Shachar, A. Blass, L. Charbin-sky, I. Aharony, L. Lifshitz, D. Lumelsky, Z. Neeman, M. Mizrachi, M. Hajouj, N. Eizenbach, E. Sela, C. S. Weiss, P. Levin, O. Benjamino, G. N. Bachar, S. Tamir, Y. Rapson, D. Suhami, E. Atar, A. A. Dror, N. R. Bogot, A. Grubstein, N. Shabshin, Y. M. Elyada, and Y. C. Eldar, "Covid-19 classification of x-ray images using deep neural networks," *Eur. Radiol.*, vol. 31, no. 12, pp. 9654–9663, Dec 2021.

[19] H. Liu, L. Wang, Y. Nan, F. Jin, Q. Wang, and J. Pu, "SDFN: Segmentation-based deep fusion network for thoracic disease classification in chest x-ray images," *Comput. Med. Imaging Graph.*, vol. 75, pp. 66–73, 2019.

[20] D. Arias-Garzón, J. A. Alzate-Grisales, S. Orozco-Arias, H. B. Arteaga-Arteaga, M. A. Bravo-Ortiz, A. Mora-Rubio, J. M. Saborit-Torres, J. Ángel Montell Serrano, M. de la Iglesia Vayá, O. Cardona-Morales, and R. Tabares-Soto, "Covid-19 detection in x-ray images using convolutional neural networks," *MLWA*, vol. 6, p. 100138, 2021.

[21] J. Irvin, P. Rajpurkar, M. Ko, Y. Yu, S. Ciurea-Ilcus, C. Chute, H. Marklund, B. Haghgoo, R. Ball, K. Shpanskaya *et al.*, "CheXpert: A large chest radiograph dataset with uncertainty labels and expert comparison," in *Proc. AAAI Artif. Intell.*, 2019, pp. 590–597.

[22] A. E. W. Johnson, T. J. Pollard, N. R. Greenbaum, M. P. Lungren, C. ying Deng, Y. Peng, Z. Lu, R. G. Mark, S. J. Berkowitz, and S. Horng, "Mimic-cxr-jpg, a large publicly available database of labeled chest radiographs," 2019.

[23] J. Shiraishi, S. Katsuragawa, J. Ikezoe, T. Matsumoto, T. Kobayashi, K. Komatsu, M. Matsui, H. Fujita, Y. Kodera, and K. Doi, "Development of a digital image database for chest radiographs with and without a lung nodule: receiver operating characteristic analysis of radiologists' detection of pulmonary nodules," *AJR Am. J. Roentgenol.*, vol. 174 1, pp. 71–4, 2000.

[24] A. Mondal, A. Agarwal, J. Dolz, and C. Desrosiers, "Revisiting cyclegan for semi-supervised segmentation," *ArXiv*, vol. abs/1908.11569, 2019.

[25] Y. Shao, Y. Gao, Y. Guo, Y. Shi, X. Yang, and D. Shen, "Hierarchical lung field segmentation with joint shape and appearance sparse learning," *IEEE Trans. Med. Imag.*, vol. 33, no. 9, pp. 1761–1780, 2014.

[26] B. Ibragimov, B. Likar, F. Pernuš, and T. Vrtovec, "Accurate landmark-based segmentation by incorporating landmark misdetections," in *IEEE ISBI*, 2016, pp. 1072–1075.

[27] T. Xu, M. Mandal, R. Long, I. Cheng, and A. Basu, "An edge-region force guided active shape approach for automatic lung field detection in chest radiographs," *Comput. Med. Imaging Graph.*, vol. 36, no. 6, pp. 452–463, 2012.

[28] M. Kholiavchenko, I. Siraztdinov, K. Kubrak, R. Badrutdinova, R. Kuleev, Y. Yuan, T. Vrtovec, and B. Ibragimov, "Contour-aware multi-label chest x-ray organ segmentation," *Int. J. Comput. Assist. Radiol. Surg.*, vol. 15, no. 3, pp. 425–436, 2020.

[29] F. Munawar, S. Azmat, T. Iqbal, C. Grönlund, and H. Ali, "Segmentation of Lungs in Chest X-Ray Image Using Generative Adversarial Networks," *IEEE Access*, vol. 8, pp. 153 535–153 545, 2020.

[30] J. C. Souza, J. O. B. Diniz, J. L. Ferreira, G. L. F. da Silva, A. C. Silva, and A. C. de Paiva, "An automatic method for lung segmentation and reconstruction in chest x-ray using deep neural networks," *Comput. Methods Programs Biomed.*, vol. 177, pp. 285–296, 2019.

[31] H.-J. Chen, S.-J. Ruan, S.-W. Huang, and Y.-T. Peng, "Lung X-ray Segmentation using Deep Convolutional Neural Networks on Contrast-Enhanced Binarized Images," *Mathematics*, vol. 8, no. 4, p. 545, 2020.

[32] L. Yao, E. Poblenz, D. Dagunts, B. Covington, D. Bernard, and K. Lyman, "Learning to diagnose from scratch by exploiting dependencies among labels," *ArXiv*, vol. abs/1710.10501, 2017.

[33] G. Huang, Z. Liu, L. Van Der Maaten, and K. Q. Weinberger, "Densely connected convolutional networks," in *IEEE CVPR*, 2017, pp. 2261–2269.

[34] H. Sak, A. W. Senior, and F. Beaufays, "Long short-term memory recurrent neural network architectures for large scale acoustic modeling," in *INTERSPEECH*, 2014, pp. 338–342.

[35] X. Wang, Y. Peng, L. Lu, Z. Lu, and R. Summers, "Tienet: Text-image embedding network for common thorax disease classification and reporting in chest x-rays," *IEEE CVPR*, pp. 9049–9058, 2018.

[36] T. K. K. Ho and J. Gwak, "Multiple feature integration for classification of thoracic disease in chest radiography," *Appl. Sci.*, vol. 9, no. 19, p. 4130, 2019.

[37] B. Chen, J. Li, X. Guo, and G. Lu, "DualCheXNet: dual asymmetric feature learning for thoracic disease classification in chest x-rays," *Biomed. Signal Process. and Control*, vol. 53, p. 101554, 2019.

[38] D. Hou, Z. Zhao, and S. Hu, "Multi-label learning with visual-semantic embedded knowledge graph for diagnosis of radiology imaging," *IEEE Access*, vol. 9, pp. 15 720–15 730, 2021.

[39] Y. Zhang, X. Wang, Z. Xu, Q. Yu, A. Yuille, and D. Xu, "When radiology report generation meets knowledge graph," *Proc Conf AAAI Artif. Intell.*, vol. 34, no. 07, pp. 12 910–12 917, Apr. 2020.

[40] L. Seyyed-Kalantari, G. Liu, M. B. A. McDermott, and M. Ghassemi, "CheXclusion: Fairness gaps in deep chest x-ray classifiers," *Pac. Symp. Biocomput.*, *Pac. Symp. Biocomput.*, vol. 26, pp. 232–243, 2021.

[41] I. Allaouzi and M. Ben Ahmed, "A novel approach for multi-label chest x-ray classification of common thorax diseases," *IEEE Access*, vol. 7, pp. 64 279–64 288, 2019.

[42] L. Luo, L. Yu, H. Chen, Q. Liu, X. Wang, J. Xu, and P.-A. Heng, "Deep mining external imperfect data for chest x-ray disease screening," *IEEE Trans. Med. Imag.*, vol. 39, no. 11, pp. 3583–3594, 2020.

[43] H. H. Pham, T. T. Le, D. Q. Tran, D. T. Ngo, and H. Q. Nguyen, "Interpreting chest x-rays via cnns that exploit hierarchical disease dependencies and uncertainty labels," *Neurocomputing*, 2021.

[44] J.-Y. Zhu, T. Park, P. Isola, and A. A. Efros, "Unpaired image-to-image translation using cycle-consistent adversarial networks," in *IEEE CVPR*, 2017, pp. 2223–2232.

[45] J. Hu, L. Shen, and G. Sun, "Squeeze-and-excitation networks," in *IEEE CVPR*, 2018, pp. 7132–7141.

[46] B. van Ginneken, M. B. Stegmann, and M. Loog, "Segmentation of anatomical structures in chest radiographs using supervised methods: a comparative study on a public database," *Med. Image Anal.*, vol. 10, no. 1, pp. 19–40, 2006.

[47] R. R. Selvaraju, M. Cogswell, A. Das, R. Vedantam, D. Parikh, and D. Batra, "Grad-cam: Visual explanations from deep networks via gradient-based localization," in *IEEE ICCV*, 2017, pp. 618–626.

[48] M. Berman, H. Jégou, A. Vedaldi, I. Kokkinos, and M. Douze, "Multi-grain: a unified image embedding for classes and instances," *ArXiv*, vol. abs/1902.05509, 2019.

[49] T. Devries and G. W. Taylor, "Improved regularization of convolutional neural networks with cutout," *ArXiv*, vol. abs/1708.04552, 2017.